Title Page

***Title*: Pixel-based machine learning and image reconstitution for dot-ELISA pathogen serodiagnosis**

***Authors*: Cleo Anastassopoulou[1], Athanasios Tsakris[1], George P. Patrinos[2,3,4], Yiannis Manoussopoulos[1,5*]**

***Authors' affiliations*:**

[1] Department of Microbiology, Medical School, University of Athens, Athens, Greece

[2] Laboratory of Pharmacogenomics and Individualized Therapy, Department of Pharmacy, School of Health Sciences, University of Patras, Patras, Greece

[3] United Arab Emirates University, Zayed Center of Health Sciences, Al-Ain, UAE

[4] United Arab Emirates University, College of Medicine and Health Sciences, Department of Pathology, Al-Ain, UAE

[5] Laboratory of Virology, Plant Protection Division of Patras, ELGO-Demeter, Patras, Greece

***For correspondence:**

E-mail: inminz@gmail.com (YM)

***Manuscript information*:**

Word count of Abstract: 247 Word count of main text: 5,716

22 Number of text pages (including references and Figure legends): 38

23 Number of Figures/Tables: 9/3

Abstract

Serological methods serve as a direct or indirect means of pathogen infection diagnosis in plant and animal species, including humans. Dot-ELISA (DE) is an inexpensive and sensitive, solid-state version of the microplate enzyme-linked immunosorbent assay, with a broad range of applications in epidemiology. Yet, its applicability is limited by uncertainties in the qualitative output of the assay due to overlapping dot colorations of positive and negative samples, stemming mainly from the inherent color discrimination thresholds of the human eye. Here, we report a novel approach for unambiguous DE output evaluation by applying machine learning-based pattern recognition of image pixels of the blot using an impartial predictive model rather than human judgment. Supervised machine learning was used to train a classifier algorithm through a built multivariate logistic regression model based on the RGB ("Red", "Green", "Blue") pixel attributes of a scanned DE output of samples of known infection status to a model pathogen (*Lettuce big-vein associated virus*). Based on the trained and cross-validated algorithm, pixel probabilities of unknown samples could be predicted in scanned DE output images which would then be reconstituted by pixels having probabilities above a cutoff that may be selected at will to yield desirable false positive and false negative rates depending on the question at hand, thus allowing for proper dot classification of positive and negative samples and, hence, accurate diagnosis. Potential improvements and diagnostic applications of the proposed versatile method that translates unique pathogen antigens to the universal basic color language are discussed.

Keywords: Dot-blot ELISA; machine learning; image analysis; serological assays; sensitivity and specificity; ROC curve; diagnostic performance.

47 ## Introduction

48 Reliable and timely diagnosis of disease-causing pathogens is of paramount importance for
49 maintaining optimal health for people, animals and the environment under the integrated One
50 Health approach (***World Health Organization, 2018***). One of the most widely used assays for
51 pathogen detection is the enzyme-linked immunosorbent assay (ELISA); in its solid-state version,
52 dot-ELISA (DE), samples are directly applied to or dotted on a nitrocellulose or nylon membrane and
53 then probed for detection by specific antibodies in a chromogenic enzymatic reaction. DE is a rapid
54 screening test that is at least as sensitive as ELISA, yet it is much cheaper and requires no special
55 equipment or working conditions. As a result, DE has been adopted in a wide array of applications,
56 ranging from disease diagnosis in humans (***Rodkvamtook et al., 2015; Subramanian et al., 2016***),
57 animals (***Fisa et al., 1997***) and plants (***Savary et al., 2012***) to microbe and toxin detection in foods
58 (***Venkataramana et al., 2015***).

59 DE is a qualitative method designed to yield either a positive or negative result in a binary
60 mode. The assay follows the ELISA architecture with similar direct or indirect versions that employ
61 primary and secondary, enzyme-conjugated monoclonal or polyclonal antibodies for targeted
62 antigen detection. In most DE applications, dots are colored by a formazan/indigo dye (***Smejkal and***
63 ***Kaul, 2001***), an *in situ* complex precipitate produced by alkaline-phosphatase (AP) 5-bromo-4-
64 chloro-3-indolyl phosphate/nitro blue tetrazolium (BCIP/NBT) substrate degradation. Output
65 evaluation after color development is empirically eye-based; consequently, positive sample
66 recognition is subjective (***Pappas, 1994; Waner et al., 1996***) and particularly error-prone. Such
67 errors may stem from overlapping dot colorations resulting from host pigment contamination (***Chen***
68 ***et al., 2012; Olkkonen and Ekroll, 2016***), or from the inherent color discrimination thresholds

concerning saturation and hue of the human eye (***Baraas and Zele, 2016; Krudy and Ladunga, 2001; Olkkonen and Ekroll, 2016; Reinhard, 2008***).

Two types of errors are possible in binary classification tests: false positives (FP) or "false alarms" and false negatives (FN) or "missing values," referring to the incorrect recognition of true negatives (TN) as positives and true positives (TP) as negatives, respectively. Proper classification of TP and TN as such is known as sensitivity and specificity, correspondingly (***Trevethan, 2017***). The two error types are inversely related, and their rates must be decided on a case-by-case basis since the arbitrary choice of one over the other could have significant epidemiologic and/or economic repercussions. For example, the detection of quarantine or dangerous pathogens by diagnostic screening tests may require the adoption of a low cutoff and high sensitivity, which could yield increased numbers of FP, but it would also increase the probability of identifying all pathogens or infected individuals (or reduce the probability of missing any), thereby preventing the release of the pathogen to the environment or to uninfected Individuals or populations. In contrast, selectively detecting a common pathogen in the presence of related species or unrelated signals (background noise) may necessitate the adoption of a high cutoff and specificity, thus reducing FP rates and costs associated with additional unnecessary diagnostic tests.

Analogously, accepting *a prior*i as positives only the evident dark spots in a DE readout will result in a high rate of missing values (FN, leaving TP undetected), whereas accepting most or all colored dots as positive will result in high rates of FP (negatives mistakenly considered positives). Either erroneous classification will influence the outcome of diagnosis. A reliable method is therefore needed for non-subjectively discriminating positive and negative samples in DE outputs. Until now, apart from some procedural attempts for improving dot quality either by removing unspecific pigmentation in plant samples (***Chen et al., 2012***), or by controlling the enzymatic

92 reaction time during incubation (***Lathwal and Sikes, 2016***), no work has been done on objectifying
93 and improving DE output interpretation. Artificial intelligence has not been explored for DE output
94 evaluation or FP/FN cutoff estimation. Herein, we describe an image pixel-based supervised
95 machine learning method for DE output evaluation. To the best of our knowledge, applying machine
96 learning to accomplish this goal using an impartial predictive model rather than human judgment is
97 novel.

98 ## Results

99

100 **The new approach for DE output evaluation: from pixel information to dot classification**
101 **and diagnosis**

102 Our approach to evaluating DE outputs and predicting the infection status of samples followed five
103 steps (*Figure 1*). First, a dot blot of a prototypic DE dataset that included known positive and
104 negative control samples was scanned at a resolution of 150 dpi and a "Pixel Information Matrix" of
105 this prototypic image was constructed with the X-Y position coordinates and RGB color information
106 for the pixels of known infection status dots. This process was followed by supervised training of a
107 classifier algorithm to predict pixel probabilities based on a random subset of the prototypic image
108 pixel information. The third step included the cross-validation of the trained classifier algorithm by
109 predicting pixel probabilities in a random subset of the original dataset not used for training, while
110 the fourth involved confusion matrix and Receiver Operating Characteristic (ROC) curve analysis and
111 selection of the appropriate cutoff value. Using the trained and validated classifier, pixel probability
112 predictions could be made after matrix construction of DE readouts of unknown samples. DE image
113 reconstitution of unknown samples at the selected cutoff allowed for proper dot classification and,
114 hence, accurate diagnosis. The entire process, after running the blot using standard methods, could
115 be completed in a few seconds.

116

117 **Harnessing pixel information of the prototypic image to train the classifier algorithm**

118 Negative controls in the prototypic DE output displayed a light olive-green color, readily
119 distinguishable from the colors of other categories of samples by the naked eye (*Figure 2*). However,
120 the color of positive controls ranged from dark purple in undiluted or low sample dilutions to light

121 violet at higher sample dilutions, with lighter colorations at higher dilutions. Color hues tended to
122 overlap between similar level dilutions, either at the high or low end (i.e., 1:50 *vs*. 1:100 or undiluted
123 *vs*. 1:2, respectively), rendering eye-based dot discrimination uncertain.

124 Image conversion of the scanned prototypic membrane resulted in an (X, Y, Z) 663 × 458 × 3,
125 3D matrix of a total of 303,654 pixels, each having unique X-Y coordinates and a particular R, G, B
126 triple integer combination defining its color. After pixel selection, the prototypic image dataset
127 comprised 65,310 observations (rows) and five variables (columns): the pixel color attributes, "Red"
128 (R), "Green" (G), and "Blue" (B), "Sample dilution" and "Infection status." In turn, the "Sample
129 dilution" variable included six levels (i.e., the undiluted state and the five tested dilutions), whilst
130 the "Infection status" variable included two levels, indicating the presence or absence of the
131 pathogen. The total number of pixels of positive and negative samples were 14,907 and 50,403,
132 respectively. The relative frequencies of pixels of the various categories of the prototypic dataset
133 according to their infection status are presented in ***Table 1***. The pixel information of the samples
134 included in the prototypic DE image was harnessed to train the classifier algorithm.

135

136 **Image pixel attributes of positive *vs*. negative samples**

137 Boxplot analysis of all pixels of samples in the prototypic DE dataset revealed unique RGB patterns
138 by infection status (***Figure 3***). In positive controls, the pixel intensity of Green was consistently lower
139 than that of the Red or Blue, whereas in negative controls the intensity of Green was equal to or
140 greater than the Blue. In the buffer alone control, the pixel intensity of Green was also slightly lower
141 than the Blue or Red. Yet, the distributions of the Green and Blue colors of the background area
142 (around the dots) category were similar (and lower than the Red) and their medians tended to be
143 equal. These patterns were preserved when considering one pixel-wide lines traversing each dot of

144 the blot at a specific Y coordinate along the corresponding X coordinates (*Figure 4*). Blue and Green
145 displayed the lowest pixel intensity in negative and positive controls, respectively, in all dilutions. In
146 the highest dilution (i.e. 1:500), although the color intensity was very low, the pattern analogies
147 were maintained. Taken together, these results suggest that pixels of dots of samples in images of
148 DE readouts contain pieces of specifically discriminative information that can be exploited for model
149 training and classification.
150

151 **The RGB model displayed the best performance characteristics for infection status**
152 **prediction**

153 Among candidate models for infection status prediction, those with B, R and G as single predictors
154 were dismissed for having the highest Akaike information criterion (AIC) values (means ± SEM =
155 29,592.0 ± 12.69, 21,554.0 ± 11.62 and 20,449.1 ± 11.42, respectively). The R+G combination also
156 had a similarly increased AIC value (19,548.1 ± 11.52), while the AIC of R+B was still elevated, but at
157 about a third of the R+G value (6,263.0 ± 9.42). Although the AIC value of the G+B pairwise
158 combination was further reduced (2,395.0 ± 9.40), it was still larger compared to that of the model
159 constructed using all predictors combined; R+G+B had the lowest AIC (2,382.2 ± 7.05) and was thus
160 selected for training the classifier algorithm. Using the selected model, the R, G, B variable
161 coefficients ± SEM were all found to be highly significant ($p<10^{-8}$) and estimated at β_1= 0.08 ± 0.015,
162 β_2= -0.72 ± 0.017, β_3= 0.54 ± 0.014, respectively, implying a minor contribution of the R variable to
163 positive pixel predictability and a substantial but reciprocal effect of the G and B variables.
164

165 **The cutoff (positive/negative threshold) of choice for diagnosis**

166 A comparison of the TP and TN pixel occurrences of the test subset to those predicted by the trained
167 classifier algorithm provided an initial validation of our approach. ***Table 2*** displays the corresponding
168 confusion matrices at five representative cutoff values (0.050, 0.135, 0.500, 0.800 and 0.950). All
169 three calculated diagnostic parameters (accuracy, sensitivity and specificity) were very high (>0.94)
170 across these cutoffs. As expected, when cutoff values increased, TP (sensitivity) and FP (false alarms)
171 decreased, while TN (specificity) and FN (missing values) increased. The relative cost of
172 misclassifying pixels at more or less stringent cutoff values becomes tangible in ***Figure 5*** that shows
173 the overlapping distributions of negative and positive pixels of the test subset of the prototypic
174 image. Yielding the lowest FP and FN rates, the 0.135 cutoff appeared to offer the best trade-off
175 among the various diagnostic performance parameters.

176 The chosen model with all three-color predictors displayed the best performance indicators
177 at the 0.135 ± 0.0022 cutoff, which was the crossing point between sensitivity (0.9888 ± 0.00009)
178 and specificity (0.9882 ± 0.00009) across the entire cutoff range (***Figure 6***). At this point the two
179 variables differed the least (Difference = 0.0006, ***Table 2***) and consequently, FP and FN rates were
180 at their nadir. Accuracy was also superior for the three-predictor model at this cutoff (0.9884 ±
181 0.00009) and inaccuracy was about 0.0116 ± 0.00009, which translates to about 230 faulty pixels
182 out of the 19593 pixels of the test subset. The excellent performance of the RGB model was also
183 evidenced by the constructed ROC curve (***Figure 7***), which revealed an Area Under the Curve (AUC)
184 value very closely approximating unity (0.9972 ± 0.00006). The optimal cutoff of 0.135 corresponds
185 to a 98.9% success rate of TP and TN (1-0.0112) predictions.

186

187 **Unambiguous dot classification and infection status prediction of unknown samples**

188 We applied our method to test plants suspected for *Lettuce big-vein associated virus* (LBVaV)
189 infection. On the original blot (***Figure 8-I***), dots of negative and positive controls displayed the light
190 olive-green and purple color, respectively, as in the prototypic DE output (***Figure 2***). Therefore, the
191 olive-green dots of unknown samples (e.g. C5:D5, C7:D7, E10:F10, and E12:F12, ***Figure 8-I***)
192 resembling negative controls (G9:H9 to G12:H12) could be classified rather easily as virus-free.
193 However, most dots of unknown samples displayed different shades of purple, ranging from
194 cyclamen to deep violet. Some dots were lighter (e.g. C4:D4 and E4:F4), comparable (e.g. A12:B12
195 and C12:D12), or darker (e.g. A1:B1, A2:B2, E8:F8 and E9:F9) than the positive controls, rendering
196 infection status determination by eye-based comparison uncertain. Application of our trained and
197 validated algorithm cleared up the confusion. After matrix conversion and pixel probability
198 prediction, the DE image of unknown samples was reconstituted at various cutoffs (***Figure 8, II-VI***),
199 revealing truly positive samples with a very high probability of success. Positive controls produced
200 a robust signal throughout the range of examined cutoffs, while negative controls did not produce
201 a signal at any considered cutoff value, as was the case for the Buffer alone negative controls.
202 ***Table 3*** shows the relative preponderance by increasing cutoff values of positive versus
203 negative pixels of unknown samples classified by the trained algorithm as well as the corresponding
204 dots calculated from pixels by accepting a mean value of 237 pixels per dot, or actually detected in
205 the reconstituted images of the DE output of unknown samples. As the cutoff increased, so did the
206 negative pixels and the corresponding dots, either calculated from the pixels or actually detected
207 (the two categories differed less than 3%, i.e., by a maximum of two dots out of the 72 of unknown
208 samples). The opposite trend was noted among positively detected pixels and the respective dots,
209 the numbers of both of which decreased as the cutoff increased.

210 At the very low cutoff of 0.050, which corresponds to low specificity and low FN rates (***Figure***
211 ***8-II***), all dots suspected to be negative due to their color hue (light olive-green in ***Figure 8-I***) were
212 classified as such. Nevertheless, some dots that were practically indistinguishable by eye from
213 positively classified pairs on the original blot also appeared to be negative (e.g. A2:B2 and C12:D12
214 *vs*. A1:B1 and A12:B12, ***Figure 8***, ***I & II***, respectively). One of the duplicate dots that gave a weak
215 positive signal at the 0.050 cutoff (E4) appeared negative at the 0.135 cutoff, which corresponds to
216 the lowest FP and FN rates (***Figure 8-III***). At the more elevated cutoff of 0.500 (***Figure 8-IV***), some
217 dots that appeared positive at the 0.135 cutoff were found to be negative (e.g. E4:F4), whereas
218 some others appeared sparsely populated by positive pixels (e.g. C8:D8, C10:D10, and E7:F7).
219 These findings are consistent with a trend towards increasing FN rates with higher cutoff
220 values as also suggested by the pixel *vs*. dot data presented in ***Table 3***. Thus, at the 0.800 cutoff
221 more positive pixels were lost from the sparsely populated dots detected at the previous cutoff;
222 some of these dots appeared to be negative (e.g. C8:D8), whereas some others were still positive
223 (e.g. C3:D3, E8:F8) (***Figure 8-V***). At the highest cutoff examined (0.995), where sensitivity and FP
224 rates are expected to be even lower, dots yielding positive signals had the highest probability of
225 being TP (***Figure 8-VI***). Here, only the darkest dots maintained their compactness, whilst most
226 sparsely populated dots detected at the previous cutoff appeared negative (e.g. C3:D3 and E8:F8).
227 To test the versatility of the method, we examined an additional DE output loaded with
228 representative dilutions of *Mirafiori lettuce big vein virus* (MilBVV), a virus unrelated to the training
229 procedure. All TP and TN samples were correctly predicted as such in the reconstituted image of the
230 scanned DE output, corroborating the versatility of the method (*Figure 9*).

231 ## Discussion

232 Diagnostic procedures for pathogens differ depending, inter alia, on the physiology of the infected
233 organism. In animal species including humans, diagnostic methods, such as nucleic acid testing,
234 allow for the direct detection of the microorganism causing the infection, typically after an
235 amplification step using, preferentially but not exclusively, the polymerase chain reaction (PCR),
236 whilst indirect methods, such as serological assays, allow for the detection of antibodies against
237 microorganism antigens. Pathogen detection in plants that lack an immune system do rely on the
238 proper detection of the pathogen, but with a couple of notable exceptions: the amplification of
239 specific targets through PCR is often proven difficult due to the presence of inhibitors in plant cells
240 (***Dorn et al., 1999; Lacroix et al., 2016; Lardeux et al., 2016; Rački et al., 2014; Schrader et al., 2012;***
241 ***Suther and Moore, 2019***) whereas, the role of the detected pathogen component is rather obscure
242 at least from the etiological point of view. In the case of viral plant pathogens, for instance, the
243 capsid protein subunits or the virus particles containing the viral genome may be detected
244 simultaneously (***Manoussopoulos and Tsagris, 2015***), indicating the establishment of the virus in its
245 host. ELISA and its inexpensive and even more sensitive, solid-state alternative DE are the methods
246 of choice for quick and reliable pathogen diagnosis in both analytical and epidemiological surveys in
247 plants (***Henry Sum et al., 2017***). DE has also been used for disease diagnosis in humans
248 (***Rodkvamtook et al., 2015; Subramanian et al., 2016***) and animals (***Fisa et al., 1997***), but mostly in
249 resource-poor settings. The major obstacle limiting the generalized applicability of the method is
250 uncertainties in DE output evaluation. In this work, we present an innovative, flexible and reliable
251 unbiased approach through which unique pathogen antigens are translated into the universal, basic
252 color language of pixels (RGB) that may be used for unambiguous DE output evaluation.

253 The proposed method relies on supervised machine learning based on a logit (logistic)
254 function that is used for prediction purposes. Machine learning is, in the broader sense, an artificial
255 intelligence procedure that enables a computer (machine) to identify patterns in big datasets on the
256 basis of previous training on known data (***Alpaydin, 2014***). Classification is a type of supervised
257 machine learning in which the learning algorithm (model) is trained on a set of rules that enable the
258 correct discrimination of items into categories (***Raschka and Mirjalili, 2017***). Depending on their
259 dimensions and resolution, raster images consist of thousands to millions of pixels containing
260 information that may be exploited for classification purposes. Raster images can be obtained easily
261 via a scanner or a similar device and, in turn, they can be readily converted into 3-D matrices and
262 datasets, holding the pixel RGB attributes and X-Y position-specifying coordinates in the image. Our
263 analysis showed that the RGB values of dots of DE outputs remained constant at different antigen
264 dilutions, providing discriminating information suitable for training in machine learning applications.
265 Differences in RGB patterns persisted even at the highest sample dilutions. Although not easily
266 discriminable by eye evaluation, samples at high dilutions had distinguishable RGB patterns from
267 those of buffer control or the background. Thus, DE blots scanned to raster images may be used in
268 machine training not only for discriminating negative from positive samples but also for
269 distinguishing between low concentration antigens and background, a task currently challenging in
270 serodiagnostic techniques.

271 To the best of our knowledge, machine learning has not been exploited for DE output
272 evaluation. The method proposed herein is simple and requires no expensive accessories to run; a
273 computer and a common portable/handheld scanner are all that is needed. The innovation at the
274 heart of the procedure lies on the exploitation of image pixels, which convey invaluable information
275 ideally suited for machine training, thereby allowing for predictions to be made for unknown pixel

276 status with measurable probabilities of success. Concerning previous work in the field, only a few
277 attempts have been made mainly based on deep learning with most of them serving to complement
278 other procedures. Thus, a deep learning approach has been employed to predict positives in ELISA
279 microplates (***Nath et al., 2018***) based on the training of an artificial neural network with microplate
280 images of known sample status and the application of the trained algorithm on microplate images
281 of unknown samples. In another report, machine learning was used as an additional step in a
282 procedure used to evaluate transformed ELISA microplate images of a Cellphone-Based Hand-Held
283 Microplate Reader (***Berg et al., 2015***). In a more recent work, an artificial intelligence system was
284 presented based on supervised deep learning that outperformed human expertise in the evaluation
285 of mammograms for breast cancer prediction, demonstrating the great promise that such systems
286 hold for diagnostic applications (***McKinney et al., 2020***).

287 ELISA is a widely used method for serodiagnosis of many important human, animal and plant
288 pathogens. One drawback of the method is the need for sophisticated and expensive laboratory
289 equipment that increases the per test cost. Another, perhaps more important disadvantage, is the
290 lack of assessment of FP and FN rates that limits its application solely to high accepted cutoff
291 (positive/negative threshold) values that correspond to increased FN, unavoidably leading to the
292 loss of TP. Indeed, lacking a reliable method for cutoff estimation, the general rule of thumb for in-
293 house ELISA microplate evaluation is the acceptance as positives only of those samples having OD
294 values either two or three times the mean of negative controls (***Crowther, 2009; Lardeux et al.,***
295 ***2016***), resulting in elevated FN rates. The situation is not less problematic for commercially available
296 ELISA kits, where manufacturers often claim comparable sensitivity and specificity to other
297 commercially available - and even licensed - ELISA kits, without elaborating further on the actual
298 diagnostic performance of the assays.

299 However, serodiagnostic methods are ever important in both clinical and phytopathological
300 practices, complementing the so-called molecular methods, exemplified by, but not restricted to,
301 hybridization and PCR, or the recently developed advanced sequencing methods known as next
302 (NGS) and third generation (TGS) sequencing. Although extremely useful as an ultra-sensitive and
303 highly specific diagnostic tool, PCR, in its various formats, needs laborious optimization and stringent
304 conditions to avoid the risk of contamination, it is costly and time-consuming with rather low
305 throughput since nucleic acid isolation and possibly reverse transcription steps have to precede it.
306 The newly developed NGS and TGS, on the other hand, are highly informative for unknown or
307 candidate pathogens, but are still very expensive for diagnostic purposes and they tend to yield
308 results that are difficult to interpret, particularly in the field of etiological host-pathogen
309 interactions. Compared to these approaches, serological methods are cheaper, require less
310 sophisticated equipment and are better suited for large surveys for the detection of known
311 pathogens in established host-pathogen relationships. Serological monitoring is essential, in
312 particular, to the design and evaluation of effective vaccination programs. DE inherits all advantages
313 of the maternal ELISA application and overcomes most of its disadvantages pertaining to cost and
314 the need for specialized equipment, rendering it an attractive alternative for serodiagnosis in
315 epidemiologic research once the problem of output evaluation is resolved.

316 Besides fully addressing in an objective and reliable manner the issue of output evaluation, a
317 major advantage of our method is that it allows for cutoff selection, thus enabling decisions to be
318 made on FP and FN acceptance rates suited to the diagnostic question at hand; furthermore,
319 estimated probability values are calculated for TP, TN, accuracy and all types of errors. The trained
320 model showed outstanding performance with high accuracy and very low FP and FN rates. The
321 accepted values of FP and FN could be easily selected through the generated ROC curve. These

322 features potentially enhance assay reproducibility by eliminating signal variability among
323 experiments arising from fluctuations in pathogen antigenicity levels or pathogen-antibody and/or
324 antibody-conjugate affinities. Our findings demonstrate the unambiguous recognition of TP and TN
325 dots in DE outputs, with certain probabilities of success, a feature missing from serodiagnostic
326 applications. Another advantage of the method is the short time it requires since no image
327 preprocessing is necessary and only a few tens of seconds, depending on the size of the image, are
328 needed to scan the processed blot and reconstitute the image from pixels above the selected
329 threshold.

330 Importantly, the method is both antigen- and control-independent. As shown in the proof-of-
331 concept experiment, the trained by the LBVaV antigen algorithm successfully detected all tested
332 dilutions of the MilBVV antigen. The two lettuce big-vein disease-associated viruses belong to
333 different classes and, as such, they have completely different molecular and particle structural
334 properties. This universality stems from the fact that there is no relationship between the kind of
335 antigen and the color produced; therefore, the method is highly versatile and appropriate for the
336 serodiagnosis of antigens of any microorganism. The algorithm classifies image pixels based on their
337 color intensity, rendering retraining and the inclusion of controls with each run unnecessary, so long
338 as the same chromogenic substrate is used. The DE control-independence offers a great advantage
339 over ELISA, where output evaluation is chiefly dependent on positive and negative controls, limiting
340 the number of samples that can be tested simultaneously and increasing cost.

341 The method can be further improved by training the algorithm with pixels from many more
342 prototypic images, covering all possible dot colorations from the full range of dilutions, with
343 emphasis on the lower end of the spectrum where positive signals turn blurry and indistinguishable
344 from the background. In theory, the training dataset could be developed by code that calculates the

345 entire range of RGB values specific for the substrate spectrum of color intensities, thereby avoiding
346 prototypic blot preparations which cannot easily cover the whole spectrum of colors. Both the
347 incorporation of more exploratory variables (e.g. dilution levels) in the training model and the
348 employment of different models, such as classification trees or random forest algorithms, could be
349 also explored. In addition, the whole procedure could be further developed to a web-based
350 application where the input will be the scanned DE image of interest and the output will be the
351 reconstituted image showing the positive and negative dots along with useful statistical metadata.
352 Application of the described method could contribute to the rapid and reliable diagnosis of
353 common or emerging pathogens in both developed and developing countries since serological
354 methods are probably the most economical and rapidly applicable methods available.

355 ## Materials and methods

356 DE output evaluation may be reduced to a binary classification problem since test samples can be
357 either infected or not infected with a given pathogen. Machine learning can be used to train a
358 classifier algorithm on known sample attributes to predict the infection status of unknown samples.
359 The following steps are key to this process: (1) prototypic DE dataset construction; (2) model
360 selection with appropriate predictive variables of high discriminative power and supervised training
361 of the classifier algorithm; (3) validation of the trained algorithm; (4) ROC curve analysis and cutoff
362 selection; (5) infection status prediction of unknown samples. An overview of the method is
363 presented in ***Figure 1***, while each step is described in the sections that follow.

364

365 **Step 1: Prototypic DE dataset construction**

366 The prototypic dataset (***Figure 2***) was constructed from a scanned output image of known positive
367 and negative controls following DE undertaken according to standard protocols using the Bioblot
368 apparatus (Bio-Rad Laboratories, Redmond, WA, USA) and commercially available LBVaV antigens
369 and specific antibodies (Prime Diagnostics, The Netherlands). Volumes of 100 µl of the following
370 types of samples were loaded on the prototypic nitrocellulose membrane: (i) virus standard
371 prepared according to the manufacturer's instructions (1 OD in ELISA at 405 nm in 30 minutes, Prime
372 Diagnostics, The Netherlands), undiluted or diluted 1:2, 1:10, 1:50, 1:100 and 1:500 in 0.01 M PBS
373 at pH=7.4 (positive controls); (ii) healthy lettuce extracts diluted 1:10 in the same phosphate buffer
374 (negative controls); and (iii) buffer alone (additional negative control for assessing background
375 noise). Positive, negative and buffer controls were randomly distributed on the 96-well apparatus
376 in twelve, eleven and 13 replicates, respectively. A blocking stage [5% skimmed milk in PBS plus
377 0.05% Tween (PBS-T)] was included after sample loading. The membrane was then processed with

378 the corresponding specific secondary, AP-conjugated antibodies. Washing for five minutes with PBS-
379 T was applied three times between each stage and after color development following incubation
380 with BCIP/NBT substrate for 15-20 minutes. The blot was then dried on Wittman paper and scanned
381 as a TIFF color image at a resolution of 150 dpi.

382 Pixels in the scanned image of the prototypic DE dataset belonged to the following four
383 categories: positive, negative, and buffer or background controls, reflecting the three types of
384 loaded material and the area around them, correspondingly. The positive category was further
385 divided into six subcategories reflecting the undiluted state or the five dilution levels of the virus
386 standard. The prototypic dataset was created by manually selecting regions of each pixel category
387 in the image (i.e., respective dots, but also including representative regions of the background) and
388 storing and processing the X-Y coordinates and RGB information of the pixels using the ImageJ
389 package (***Schneider et al., 2012***).

390

391 **Step 2: Model selection and supervised training of the classifier algorithm**

392 The constructed prototypic DE dataset was used for model variable exploration and machine
393 learning. Statistical analysis and training were performed by programming the proper library or
394 function of the "R" statistical program (***R Core Team, 2018***). A multivariable logistic regression
395 model was employed in which the log odds of infection status (i.e., "Yes" or "No") was the
396 dependent variable and the R, G, B attributes of the pixels were the predictor variables. The
397 generalized linear model had the following form (***Agresti, 2013***):

398 $$\ln\left({\pi(x)}\big/{1-\pi(x)}\right) = \alpha + \beta_1 x_R + \beta_2 x_G + \beta_3 x_B + \beta_4 x_{Dil}, \text{ where}$$

399 the letters α, β_1, β_2, β_3, β_4 represent the intercept and corresponding parameters of the x_R (Red), x_G

400 (Green), x_B (Blue), x_{Dil} (Dilution) variables. Successful event (positive pixel) probabilities can be

401 obtained from the model according to the equation:

402 $$\pi(\chi) = \frac{e^{\alpha+\beta_1 x_R+\beta_2 x_G+\beta_3 x_B+\beta_4 x_{Dil}}}{1+e^{\alpha+\beta_1 x_R+\beta_2 x_G+\beta_3 x_B+\beta_4 x_{Dil}}}.$$

403 To select the most appropriate predictors, the AIC value of different logit models was considered.

404 Since AIC provides an estimate of the relative amount of information lost by a given model, the less

405 information a model loses, the higher the quality of that model (***Akaike, 1974; Hosmer et al., 2013***).

406 Each model was constructed using a single predictor (i.e., R, G, or B), each of all possible pairwise

407 predictor combinations (i.e., R+G, R+B, or G+B), or all three predictors combined (i.e., R+G+B). In all

408 cases, the 'Dilution' category and variable interactions were excluded at this stage for simplicity.

409 Logistic regression was performed using the "glm" function in "R" (***R Core Team, 2018***).

410

411 **Step 3: Validation of the trained algorithm**

412 Training was performed using the best fit logistic model and the prototypic subset. To avoid data

413 overfitting (overtraining), an additional cross-validation step was undertaken using two random

414 subsets obtained from the prototypic DE dataset by employing the "caTools" library (***Tuszynski,***

415 ***2018***) in R (***R Core Team, 2018***): a training subset holding about 70% of pixels and a test subset

416 holding the rest 30% of pixels of the original (prototypic) image (***Figure 2***). For validation, predictions

417 on the "training" and "testing" subsets were made by the "predict" function in "R" based on the

418 logistic training model and the training subset. Confusion matrices were constructed at 0.01

419 intervals for each randomly created dataset and critical diagnostic parameters, such as the Cutoff,

420 Sensitivity, Specificity, Accuracy and Error, were calculated as follows: Sensitivity was estimated as

421 TP/(TP+FN), Specificity as TN/(TN+FP), Accuracy as (TP+TN)/(TP+TN+FP+FN) and Error as
422 (FP+FN)/(TP+TN+FP+FN). The optimal cutoff was estimated as the probability at which Sensitivity
423 and Specificity differed the least. The above process was repeated 100 times using code written in
424 "R" (***R Core Team, 2018***). For validation purposes, the same diagnostic parameters of each random
425 dataset were obtained using the "performance" function of the "ROCR" library (***Sing et al., 2005***) in
426 "R" (***R Core Team, 2018***).

427 To obtain 95% confidence intervals (CI) for the mean of each variable, the corresponding
428 dataset containing a random sample (n=100) of each of the parameters was bootstrapped 10,000
429 times using the "boot" library (***Davison and Hinkley, 1997***) in "R" (***R Core Team, 2018***). To ensure
430 reproducibility and integrity of the used datasets, which could be influenced by stochasticity
431 introduced during the dataset splitting, each of the 100 splitting events was controlled by the R base
432 "set.seed" function, taking incrementally integer arguments from 1 to 100, with each integer
433 corresponding to one splitting event.

434

435 **Step 4: ROC curve analysis and cutoff selection**

436 The ROC curve of each dataset was constructed using the "ROCR" library (***Sing et al., 2005***) in "R".
437 Representative cutoffs and the corresponding Sensitivity and Specificity values were obtained from
438 constructed ROC curves. Optimum cutoff selection and corresponding variables were obtained by
439 finding the minimum absolute difference between "Sensitivity" and "Specificity" that coincided with
440 crossing point of the two variables. AUC was calculated at the selected cutoff of 0.135.

441

442 **Step 5: Infection status prediction of unknown samples**

443 To investigate the diagnostic performance of the method and its applicability to real-world
444 situations, we used lettuce plants grown in a field infested with the fungus *Olpidium virulentus,* a
445 known vector of LBVaV (***Roggero et al., 2000***). Sap from lettuce leaves was extracted (1g/10 ml) in
446 phosphate buffer (0.01M, pH=7.4) and centrifuged at low speed (10,000g) for ten minutes. The
447 supernatant was collected and loaded onto nitrocellulose membranes, which were processed with
448 LBVaV-specific, AP-conjugated antibodies and NBT/BCIP substrate as described previously. To
449 further examine the detection performance of the method for an antigen other than that on which
450 the training model was based, we followed the described procedure for a DE blot loaded with
451 representative dilutions of commercially available MilBVV positive and negative controls (Prime
452 Diagnostics, The Netherlands). After color development and washing, dried sheets in each case were
453 scanned into color images and the corresponding matrices with pixel coordinate information and
454 RGB values were obtained by programming the "sys", "NumPy" and "pandas" libraries in Python
455 ver. 3.5 (***Oliphant, 2007; van der Walt et al., 2011; Wes McKinney, 2010***). Pixel probabilities of the
456 unknown sample datasets were predicted using the "predict" function in "R" (***R Core Team, 2018***)
457 and the trained subset logistic model. DE images of unknown samples were reconstituted at a broad
458 range of cutoffs to investigate their effects on infection status predictions. Pictures were
459 reconstituted by programming the "ggplot2" library (***Wickham, 2016***) in "R" (***R Core Team, 2018***)
460 using pixels falling above the representative cutoffs of 0.05, 0.16, 0.5, 0.8 and 0.995 obtained from
461 the ROC curve or from the described explorative confusion matrices, along with the corresponding
462 pixel X-Y coordinates. The DE image of MiLBVV dilutions was reconstituted at the 0.13 cutoff.

463

464 **Predicted pixels' classification and dot infection status**

465 To further examine the association between predicted pixels' classification and dot infection status,
466 we manually collected all X-Y coordinates and RGB information of the dots of the unknown samples
467 using ImageJ (***Schneider et al., 2012***). Subsequently, we made predictions using the trained
468 algorithm and calculated the total positively and negatively classified pixels across the range of
469 representative cutoffs, i.e. at 0.050, 0.135, 0.500, 0.800 and 0.995. Then, using the mean number of
470 pixels per dot, we estimated the positive and negative dots corresponding to the reconstituted
471 pictures of each of the examined cutoffs.
472

Table 1. Relative frequencies of pixel categories of the prototypic dataset by infection status.

Sample type	Dilution level	No. of replicates	Number of pixels
Positive controls	No dilution	12	3189
Positive controls	1:2	12	2780
Positive controls	1:10	12	2428
Positive controls	1:50	12	1804
Positive controls	1:100	12	2523
Positive controls	1:500	12	2183
Positive pixels subtotal			**14907**
Background (area around dots)	NA	NA	44993
Buffer alone	No dilution	13	2426
Negative controls	No dilution	11	2984
Negative pixels subtotal			**50403**
Total			**65310**

NA, Not Applicable

473

Table 2. Comparison of diagnostic performance indicators at representative cutoffs generated from the respective confusion matrices of observed against predicted by the trained classifier algorithm pixel status in the test subset (n= 19,593).

Cutoff	Confusion matrices of pixel status				Diagnostic performance	
0.050			Predicted		Accuracy	0.9817
			Negative	Positive	Sensitivity	0.9922
	Observed	Negative	14798	323	Specificity	0.9786
		Positive	35	4437	Difference	0.0136
0.135			Predicted		Accuracy	0.9884
			Negative	Positive	Sensitivity	0.9888
	Observed	Negative	14943	178	Specificity	0.9882
		Positive	50	4422	Difference	0.0006
0.500			Predicted		Accuracy	0.9943
			Negative	Positive	Sensitivity	0.9832
	Observed	Negative	15085	36	Specificity	0.9976
		Positive	75	4397	Difference	0.0144
0.800			Predicted		Accuracy	0.9923
			Negative	Positive	Sensitivity	0.9685
	Observed	Negative	15112	9	Specificity	0.9994
		Positive	141	4331	Difference	0.0309
0.995			Predicted		Accuracy	0.9882
			Negative	Positive	Sensitivity	0.9488
	Observed	Negative	15118	3	Specificity	0.9998
		Positive	229	4243	Difference	0.0510

478 **Table 3.** Relative numbers of predicted positive and negative pixels of dots of the DE output of

479 unknown samples and the corresponding numbers of dots calculated from pixels or counted in the

480 reconstituted images by increasing cutoff values (related to *Figure 8*).

			Dots (n)			
	Pixels (n)*		Calculated from pixels**		Detected on reconstituted images	
Cutoff	Positive	Negative	Positive	Negative	Positive	Negative
0.050	14782	7939	62	34	60	36
0.135	14281	8440	60	36	59	37
0.500	12691	10030	54	42	53	43
0.800	11377	11344	48	48	46	50
0.995	9874	12847	42	54	43	53

481 *. The total number of pixels selected from the 96 dots was 22,721.

482 **. Dots were calculated from pixels by accepting a mean value of 237 pixels per dot. Images' resolution

483 was approximately 5.9 pixels/mm.

484 **FIGURE LEGENDS**

485

486 **Figure 1.** Overview of the proposed machine learning approach for DE output evaluation that
487 harnesses pixel information for dot classification and diagnosis in merely a few hundreds of seconds
488 after running the blot using standard methods. The DE output is first scanned (at a resolution of 150
489 dpi) and the prototypic image is converted to a matrix, holding pixel position and color information
490 for all pixels contained in the dots (1). The matrix is then randomly tessellated into a training and
491 testing dataset at a 70:30 ratio. Next, training of the classifier algorithm (2) is supervised by a logistic
492 model of choice which, following validation (3), is used for infection status predictions on the testing
493 subset. ROC curve analysis allows for selection of an appropriate cutoff (4). The procedure of
494 scanning the blot and harnessing its pixel information is repeated on a DE of unknown samples (5).
495 Pixel probabilities of the unknown samples are predicted by the trained classifier and a new image
496 of the blot, with dots consisting of pixels with probabilities above the selected cutoff, is
497 reconstituted, allowing for proper dot classification and, hence, unambiguous diagnosis.

498

499 **Figure 2.** Scanned image (at 150 dpi resolution) of the prototypic DE output used for training the
500 classifier algorithm. Positive, negative and buffer controls were randomly distributed on the
501 membrane in 12, 11 and 13 replicates, respectively. The letters on top of the dots denote the Buffer
502 (B) and the negative (N) controls, while the numbers 1, 2, 10, 50, 100, and 500 denote no dilution,
503 or 1:2, 1:10, 1:50, 1:100, and 1:500 dilutions of the positive control (LBVaV virus standard, Prime
504 Diagnostics, The Netherlands), respectively.

505

506 **Figure 3.** Box plots of relative color intensity of prototypic blot pixels of different categories.
507 Numbers above the plots indicate the undiluted status (1) or dilutions of the positive control (1:2,
508 1:10, 1:50, 1:100, and 1:500), while letters indicate the Buffer alone (B), background area around
509 the dots (BGR), and Negative (N) controls.

510

511 **Figure 4.** RGB pixel intensity *vs.* dot coloration patterns in a perceived one pixel-wide line. A four
512 pixel-wide line (~6 pixels per mm) is actually shown here traversing the fourth row of the prototypic
513 blot image at a representative point of the Y-axis (Y=204). Each dot on the blot is a raster or bitmap
514 image of approximately 200 pixels. Numbers above the dots denote the undiluted status (1) or
515 dilution factor of positive samples. N and B denote negative and buffer controls, respectively.

516

517 **Figure 5.** Histogram of stacked bars and the corresponding density curves showing the frequencies
518 and density of classified pixels of the test subset of the prototypic image as negative (blue) or
519 positive (orange). The length of each bar is proportional to the number of classified pixels at each
520 probability class (defined by the bar width). The picture zooms at the range of probabilities between
521 0.05 and 0.99, concealing the high proportions of negatives (near zero) and positives (near one) (see
522 Supplementary Figure 1) to emphasize the overlapping between misclassified pixels. The black
523 vertical line crossing at the selected cutoff (0.135 in this case) divides the plot into two halves that
524 represent negative (below the cutoff) and positive (above the cutoff) predicted pixels. As the vertical
525 line moves to the right (increasing cutoff), more TN are collected (blue bars to the right) at the cost
526 of considering some orange bars (TP) as negatives (TN or specificity increase). When the line moves
527 to the left (decreasing cutoff) more TP (orange bars) are detected at the cost of misconsidering some
528 blue bars (TN) as orange (positives) (TP or sensitivity increase). Selecting the appropriate cutoff for

529 each diagnostic case is unavoidably a compromise that minimizes the effects of the least important
530 error type.
531
532 **Figure 6.** Sensitivity and Specificity of the test dataset across the entire cutoff range (0 – 1). The
533 crossing point (red dot) of the two curves indicates the selected cutoff value (0.135), at the zenith
534 of the TP (0.9888) and TN rates (0.9882), which corresponds to the nadir of FP and FN rates (1-
535 0.9882=0.0118 and 1-0.9888=0.0112, respectively).
536
537 **Figure 7.** Sensitivity *vs.* 1-Specificity (FP) plot of the test dataset (left panel), zooming into the top
538 left-hand corner of the plot region (right panel). The blue shaded part of the plot in the left shows
539 the Area Under the Curve (AUC). The selected cutoff of 0.135 (red dot) corresponds to a 98.9%
540 success rate of TP and 98.8 % (1-0.0118) TN predictions.
541
542 **Figure 8.** Scanned image of a DE output of lettuce samples suspected for LBVaV infection (I) and the
543 corresponding images reconstituted from pixels applying cutoffs of 0.050 (II) 0.135 (III), 0.500 (IV),
544 0.800 (V) and 0.995 (VI). Duplicates of 36 samples of unknown infection status were loaded in [(A-
545 F):(1-12)]. Lanes G and H contain duplicates of positive (+) controls (1-4), Buffer only (5-8), and
546 negative (-) controls (9-12). Framed in red are two of the sets of dots of ambiguous diagnosis that
547 appear similar in the original DE output (I). In the reconstituted images, however, where pixel
548 information of dots has been harnessed, it becomes clear that dots A12:B12 are positive and
549 C12:D12 negative.

550 **Figure 9.** Scanned image of a DE output of positive and negative controls of MilBVV (I) and
551 reconstituted image (II) made by pixels with predicted probabilities above the 0.135 cutoff based
552 on the LBVaV-trained model. Lanes A and B show duplicates of undiluted (1 and 5), and 1:5 (2) 1:10
553 (3) and 1:50 (4) dilutions of the positive control of MilBVV. Dots 6 and 7 are buffer only controls.
554 Dots 8 to 12 contain the negative control of MilBVV undiluted (8,12), and at 1:5 (9), 1:10 (10), and
555 1:50 (11) dilutions. The translation of unique antigens, of MilBVV here, to the universal basic color
556 language allows for its detection by the algorithm (model) we built, even though it was trained on
557 the basis of a different virus, LBVaV.

Author contributions

Cleo Anastassopoulou, Visualization, Methodology, Supervision, Project administration, Writing—original draft, Writing—review and editing; Athanasios Tsakris, Resources, Writing—review and editing; George P. Patrinos, Resources, Writing—review and editing; Yiannis Manoussopoulos, Conceptualization, Data curation, Software (Code development), Formal analysis, Validation, Investigation, Resources, Visualization, Methodology, Writing—original draft, Writing—review and editing.

Author ORCIDs

Cleo Anastassopoulou https://orcid.org/0000-0001-7666-9198

Athanasios Tsakris https://orcid.org/0000-0003-0656-4715

George P. Patrinos https://orcid.org/0000-0002-0519-7776

Yiannis Manoussopoulos https://orcid.org/0000-0002-6065-7368

572 # References

573 **Agresti A**. 2013. *Categorical data analysis, 3rd edn.* Wiley, Hoboken, NJ

574 **Akaike H**. 1974. A New Look at the Statistical Model Identification. *IEEE Transactions on Automatic*
575 *Control* **19**:716–723

576 **Alpaydin E**. 2014. *Introduction to machine learning*. The MIT Press, Cambridge, Massachusetts

577 **Baraas RC**, Zele AJ. 2016. Psychophysical Correlates of Retinal Processing. In: Kremers J, Baraas RC,
578 Marshall NJ, eds. *Human Color Vision*. Springer International Publishing, Cham

579 **Berg B**, Cortazar B, Tseng D, Ozkan H, Feng S, Wei Q, Chan RY-L, Burbano J, Farooqui Q, Lewinski
580 M, Di Carlo D, Garner OB, Ozcan A. 2015. Cellphone-Based Hand-Held Microplate Reader for
581 Point-of-Care Testing of Enzyme-Linked Immunosorbent Assays. *ACS nano* **9**:7857–7866.
582 doi: 10.1021/acsnano.5b03203, PMID: 26159546

583 **Chen Z**, Liu J, Zeng M, Wang Z, Yu D, Yin C, Jin L, Yang S, Song B. 2012. Dot immunobinding assay
584 method with chlorophyll removal for the detection of southern rice black-streaked dwarf virus.
585 *Molecules (Basel, Switzerland)* **17**:6886–6900. doi: 10.3390/molecules17066886, PMID:
586 22669043

587 **Crowther JR**. 2009. *The ELISA guidebook, 2nd edn.* Humana; [London : Springer, Totowa, N.J.

588 **Davison AC**, Hinkley D v. 1997. *Bootstrap methods and their application*. Cambridge University
589 Press, Cambridge

590 **Dorn PL**, Engelke D, Rodas A, Rosales R, Melgar S, Brahney B, Flores J, Monroy C. 1999. Utility of
591 the polymerase chain reaction in detection of Trypanosoma cruzi in Guatemalan Chagas'
592 disease vectors. *The American journal of tropical medicine and hygiene* **60**:740–745.
593 doi: 10.4269/ajtmh.1999.60.740, PMID: 10344645

594 **Fisa R**, Gállego M, Riera C, Aisa MJ, Valls D, Serra T, Colmenares M de, Castillejo S, Portús M. 1997.
595 Serologic diagnosis of canine leishmaniasis by dot-ELISA. *Journal of veterinary diagnostic*
596 *investigation* **9**:50–55. doi: 10.1177/104063879700900109, PMID: 9087925
597 **Henry Sum MS**, Yee SF, Eng L, Poili E, Lamdin J. 2017. Development of an Indirect ELISA and Dot-
598 Blot Assay for Serological Detection of Rice Tungro Disease. *BioMed research international*
599 **2017**:3608042. doi: 10.1155/2017/3608042, PMID: 29201901
600 **Hosmer DW**, Lemeshow S, Sturdivant RX. 2013. *Applied logistic regression*. Wiley, Hoboken New
601 Jersey
602 **Krudy Á**, Ladunga K. 2001. Measuring Wavelength Discrimination Threshold Along The Entire
603 Visible Spectrum. *Periodica Polytechnica Ser. Mech. Eng.* **45**:41–48
604 **Lacroix C**, Renner K, Cole E, Seabloom EW, Borer ET, Malmstrom CM. 2016. Methodological
605 Guidelines for Accurate Detection of Viruses in Wild Plant Species. *Applied and environmental*
606 *microbiology* **82**:1966–1975. doi: 10.1128/AEM.03538-15, PMID: 26773088
607 **Lardeux F**, Aliaga C, Depickère S. 2016. Bias due to methods of parasite detection when estimating
608 prevalence of infection of Triatoma infestans by Trypanosoma cruzi. *Journal of vector ecology :*
609 *journal of the Society for Vector Ecology* **41**:285–291. doi: 10.1111/jvec.12224, PMID: 27860015
610 **Lathwal S**, Sikes HD. 2016. Assessment of colorimetric amplification methods in a paper-based
611 immunoassay for diagnosis of malaria. *Lab on a chip* **16**:1374–1382. doi: 10.1039/c6lc00058d,
612 PMID: 27001468
613 **Manoussopoulos IN**, Tsagris M. 2015. Native Electrophoresis and Western Blot Analysis (NEWeB):
614 Methods and Applications. *Methods in molecular biology (Clifton, N.J.)* **1312**:343–353.
615 doi: 10.1007/978-1-4939-2694-7_35, PMID: 26044016

616 **McKinney SM**, Sieniek M, Godbole V, Godwin J, Antropova N, Ashrafian H, Back T, Chesus M,
617 Corrado GC, Darzi A, Etemadi M, Garcia-Vicente F, Gilbert FJ, Halling-Brown M, Hassabis D,
618 Jansen S, Karthikesalingam A, Kelly CJ, King D, Ledsam JR, Melnick D, Mostofi H, Peng L, Reicher
619 JJ, Romera-Paredes B, Sidebottom R, Suleyman M, Tse D, Young KC, Fauw J de, Shetty S. 2020.
620 International evaluation of an AI system for breast cancer screening. *Nature* **577**:89–94.
621 doi: 10.1038/s41586-019-1799-6, PMID: 31894144
622 **Nath S**, Sarcar S, Chatterjee B, Chourashi R, Chatterjee NS. 2018. Smartphone camera-based
623 analysis of ELISA using artificial neural network. *IET Computer Vision* **12**:826–833.
624 doi: 10.1049/iet-cvi.2017.0585
625 **Oliphant TE**. 2007. Python for Scientific Computing. *Computing in science & engineering* **9**:10–20.
626 doi: 10.1109/MCSE.2007.58
627 **Olkkonen M**, Ekroll V. 2016. Color Constancy and Contextual Effects on Color Appearance. In:
628 Kremers J, Baraas RC, Marshall NJ, eds. *Human Color Vision*. Springer International Publishing,
629 Cham
630 **Pappas MG**. 1994. *The Biotech Business Handbook*. Springer Science+Business Media, LLC, New
631 York
632 **R Core Team**. 2018. *R: A Language and Environment for Statistical Computing*. R Foundation for
633 Statistical Computing, Vienna, Austria
634 **Rački N**, Dreo T, Gutierrez-Aguirre I, Blejec A, Ravnikar M. 2014. Reverse transcriptase droplet
635 digital PCR shows high resilience to PCR inhibitors from plant, soil and water samples. *Plant*
636 *methods* **10**:42. doi: 10.1186/s13007-014-0042-6, PMID: 25628753

637 **Raschka S**, Mirjalili V. 2017. *Python machine learning: Machine learning and deep learning with*
638 *Python, scikit-learn, and TensorFlow / Sebastian Raschka & Vahid Mirjalili*. Packt Publishing,
639 Birmingham, UK
640 **Reinhard E**. 2008. *Color imaging: Fundamentals and applications*. A.K. Peters, Wellesley Mass
641 **Rodkvamtook W**, Zhang Z, Chao C-C, Huber E, Bodhidatta D, Gaywee J, Grieco J, Sirisopana N,
642 Kityapan M, Lewis M, Ching W-M. 2015. Dot-ELISA Rapid Test Using Recombinant 56-kDa
643 Protein Antigens for Serodiagnosis of Scrub Typhus. *The American journal of tropical medicine*
644 *and hygiene* **92**:967–971. doi: 10.4269/ajtmh.14-0627, PMID: 25802430
645 **Roggero P**, Ciuffo M, Vaira AM, Accotto GP, Masenga V, Milne RG. 2000. An Ophiovirus isolated
646 from lettuce with big-vein symptoms. *Archives of virology* **145**:2629–2642, PMID: 11205109
647 **Savary S**, Ficke A, Aubertot J-N, Hollier C. 2012. Crop losses due to diseases and their implications
648 for global food production losses and food security. *Food Security* **4**:519–537.
649 doi: 10.1007/s12571-012-0200-5
650 **Schneider CA**, Rasband WS, Eliceiri KW. 2012. NIH Image to ImageJ: 25 years of image analysis.
651 *Nature methods* **9**:671–675. doi: 10.1038/nmeth.2089
652 **Schrader C**, Schielke A, Ellerbroek L, Johne R. 2012. PCR inhibitors - occurrence, properties and
653 removal. *Journal of applied microbiology* **113**:1014–1026. doi: 10.1111/j.1365-
654 2672.2012.05384.x, PMID: 22747964
655 **Sing T**, Sander O, Beerenwinkel N, Lengauer T. 2005. ROCR: visualizing classifier performance in R.
656 *Bioinformatics (Oxford, England)* **21**:3940–3941. doi: 10.1093/bioinformatics/bti623, PMID:
657 16096348
658 **Smejkal GB**, Kaul AC. 2001. Stability of Nitroblue Tetrazolium-based Alkaline Phosphatase
659 Substrates. *The Journal of Histochemistry & Cytochemistry* **49**:1189–1190

660 **Subramanian S**, Mahadevan A, Satishchandra P, Shankar SK. 2016. Development of a dot blot
661 assay with antibodies to recombinant "core" 14-3-3 protein: Evaluation of its usefulness in
662 diagnosis of Creutzfeldt-Jakob disease. *Annals of Indian Academy of Neurology* **19**:205–210.
663 doi: 10.4103/0972-2327.176867, PMID: 27293331
664 **Suther C**, Moore MD. 2019. Quantification and discovery of PCR inhibitors found in food matrices
665 commonly associated with foodborne viruses. *Food Science and Human Wellness* **8**:351–355.
666 doi: 10.1016/j.fshw.2019.09.002
667 **Trevethan R**. 2017. Sensitivity, Specificity, and Predictive Values: Foundations, Pliabilities, and
668 Pitfalls in Research and Practice. *Frontiers in public health* **5**:307.
669 doi: 10.3389/fpubh.2017.00307, PMID: 29209603
670 **Tuszynski J**. 2018. *caTools: Tools: moving window statistics, GIF, Base64, ROC AUC, etc*
671 **van der Walt S**, Colbert SC, Varoquaux G. 2011. The NumPy Array: A Structure for Efficient
672 Numerical Computation. *Computing in science & engineering* **13**:22–30.
673 doi: 10.1109/MCSE.2011.37
674 **Venkataramana M**, Rashmi R, Uppalapati SR, Chandranayaka S, Balakrishna K, Radhika M, Gupta
675 VK, Batra HV. 2015. Development of sandwich dot-ELISA for specific detection of Ochratoxin A
676 and its application on to contaminated cereal grains originating from India. *Frontiers in*
677 *microbiology* **6**:511. doi: 10.3389/fmicb.2015.00511, PMID: 26074899
678 **Waner T**, Naveh A, Wudovsky I, Carmichael LE. 1996. Assessment of maternal antibody decay and
679 response to canine parvovirus vaccination using a clinic-based enzyme-linked immunosorbent
680 assay. *Journal of veterinary diagnostic investigation* **8**:427–432.
681 doi: 10.1177/104063879600800404, PMID: 8953526

Wes McKinney. 2010. Data Structures for Statistical Computing in Python. In: Stéfan van der Walt, Jarrod Millman, eds. *Proceedings of the 9th Python in Science Conference*

Wickham H. 2016. *Ggplot2: Elegrant graphics for data analysis / Hadley Wickham ; with contributions by Carson Sievert*. Springer, Switzerland

World Health Organization. 2018. One Health. http://www.who.int/features/qa/one-health/en/

Figure 1

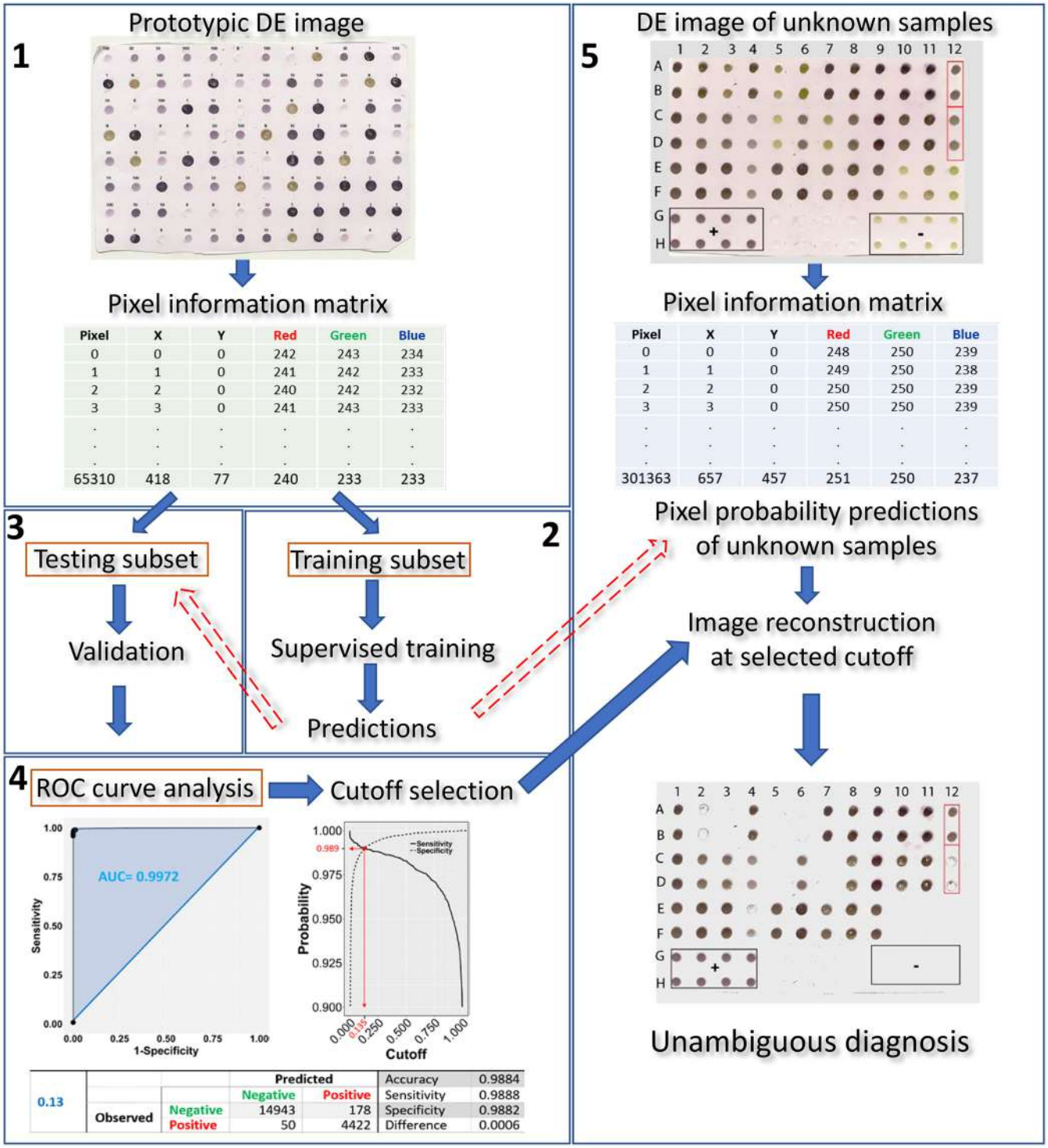
1
Prototypic DE image
Pixel information matrix
Pixel X Y Red Green Blue
0 0 0 242 243 234
1 1 0 241 242 233
2 2 0 240 242 232
3 3 0 241 243 233
65310 418 77 240 233 233
3
Testing subset
Validation
2
Training subset
Supervised training
Predictions
4
ROC curve analysis
Cutoff selection
AUC= 0.9972
Sensitivity
1-Specificity
Probability
Cutoff
Sensitivity
Specificity
0.989
0.139
Predicted
Negative Positive
0.13
Observed
Negative 14943 178
Positive 50 4422
Accuracy 0.9884
Sensitivity 0.9888
Specificity 0.9882
Difference 0.0006
5
DE image of unknown samples
Pixel information matrix
Pixel X Y Red Green Blue
0 0 0 248 250 239
1 1 0 249 250 238
2 2 0 250 250 239
3 3 0 250 250 239
301363 657 457 251 250 237
Pixel probability predictions of unknown samples
Image reconstruction at selected cutoff
Unambiguous diagnosis

Figure 2

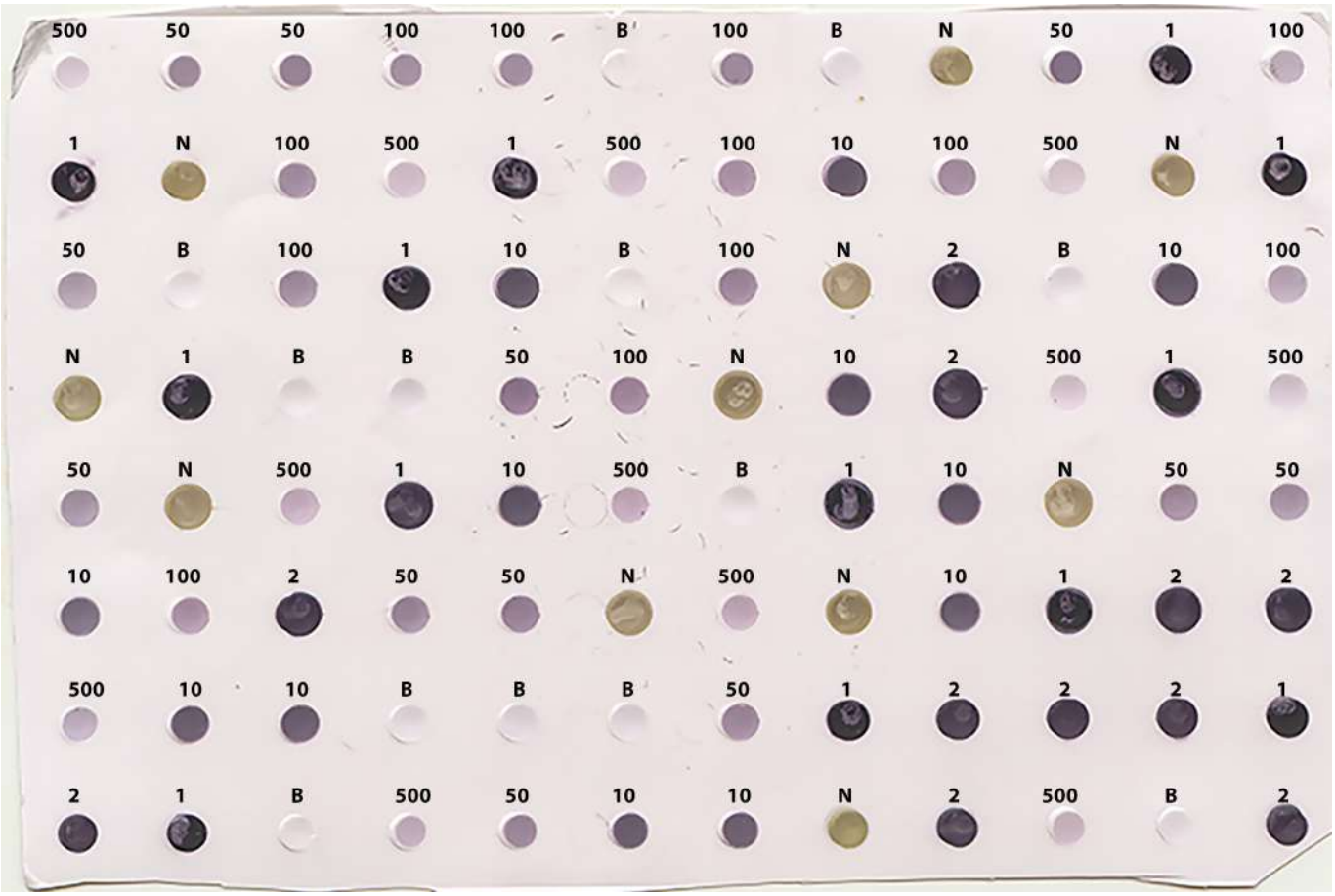
500 50 50 100 100 B 100 B N 50 1 100
1 N 100 500 1 500 100 10 100 500 N 1
50 B 100 1 10 B 100 N 2 B 10 100
N 1 B B 50 100 N 10 2 500 1 500
50 N 500 1 10 500 B 1 10 N 50 50
10 100 2 50 50 N 500 N 10 1 2 2
500 10 10 B B B 50 1 2 2 2 1
2 1 B 500 50 10 10 N 2 500 B 2

Figure 3

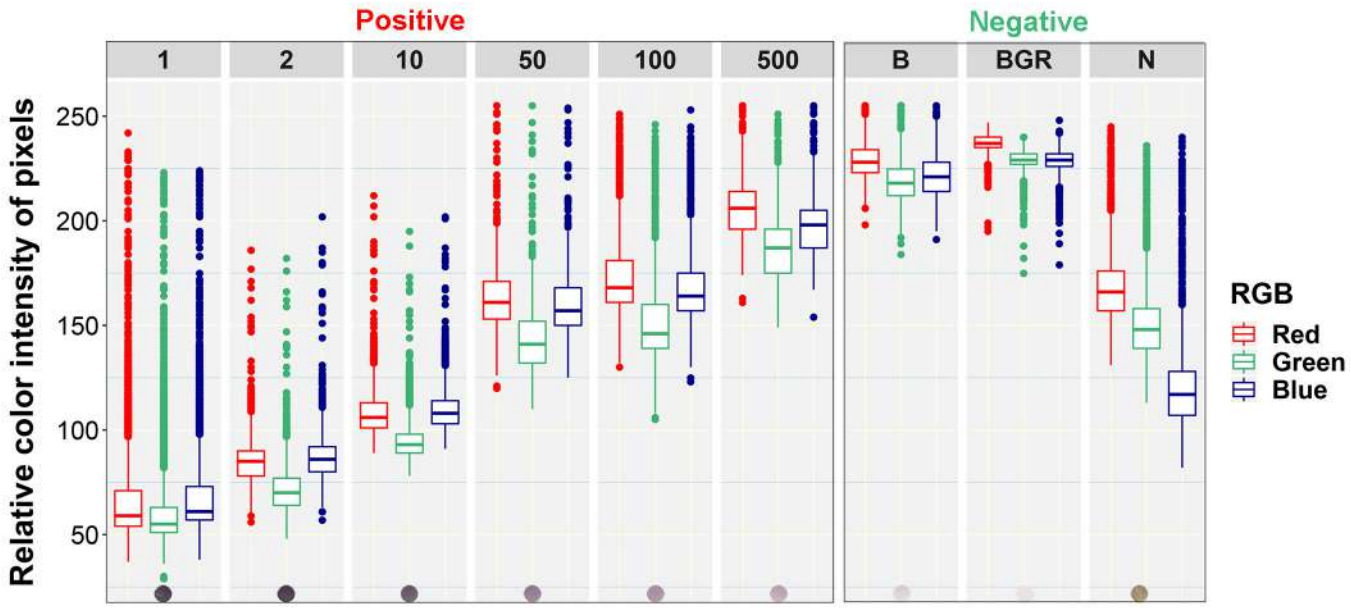
Positive
Negative
1
2
10
50
100
500
B
BGR
N
Relative color intensity of pixels
250
200
150
100
50
RGB
Red
Green
Blue

Figure 4

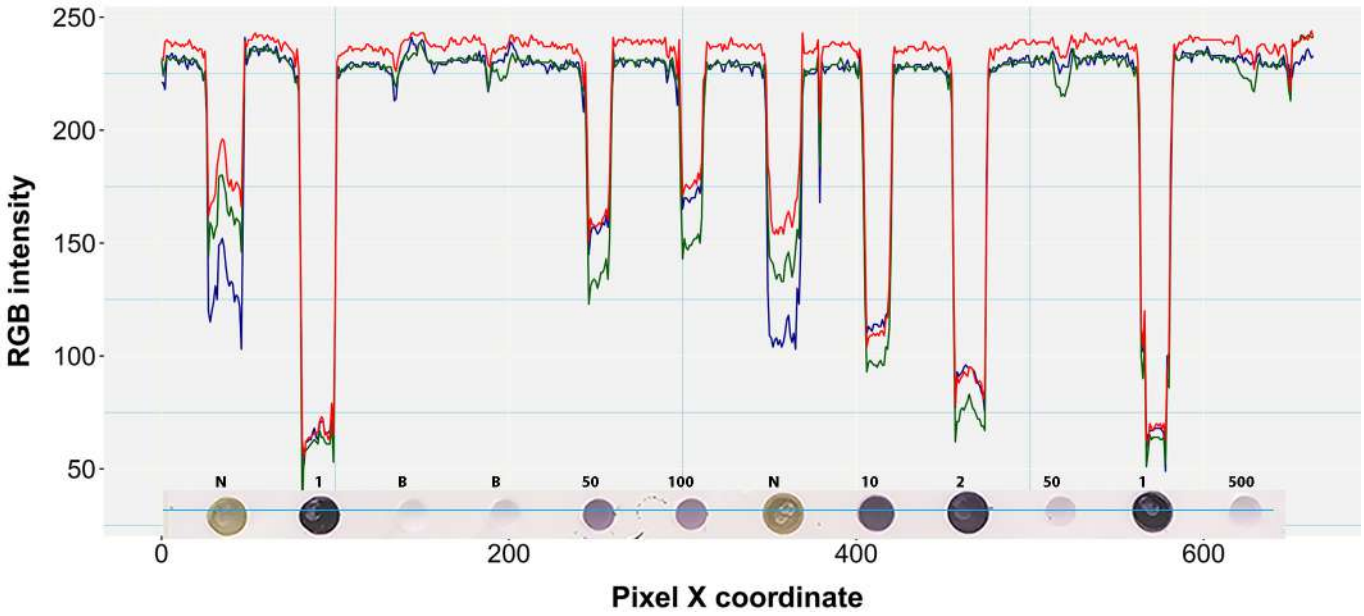
RGB intensity
250
200
150
100
50
N
1
B
B
50
100
N
10
2
50
1
500
0
200
400
600
Pixel X coordinate

Figure 5

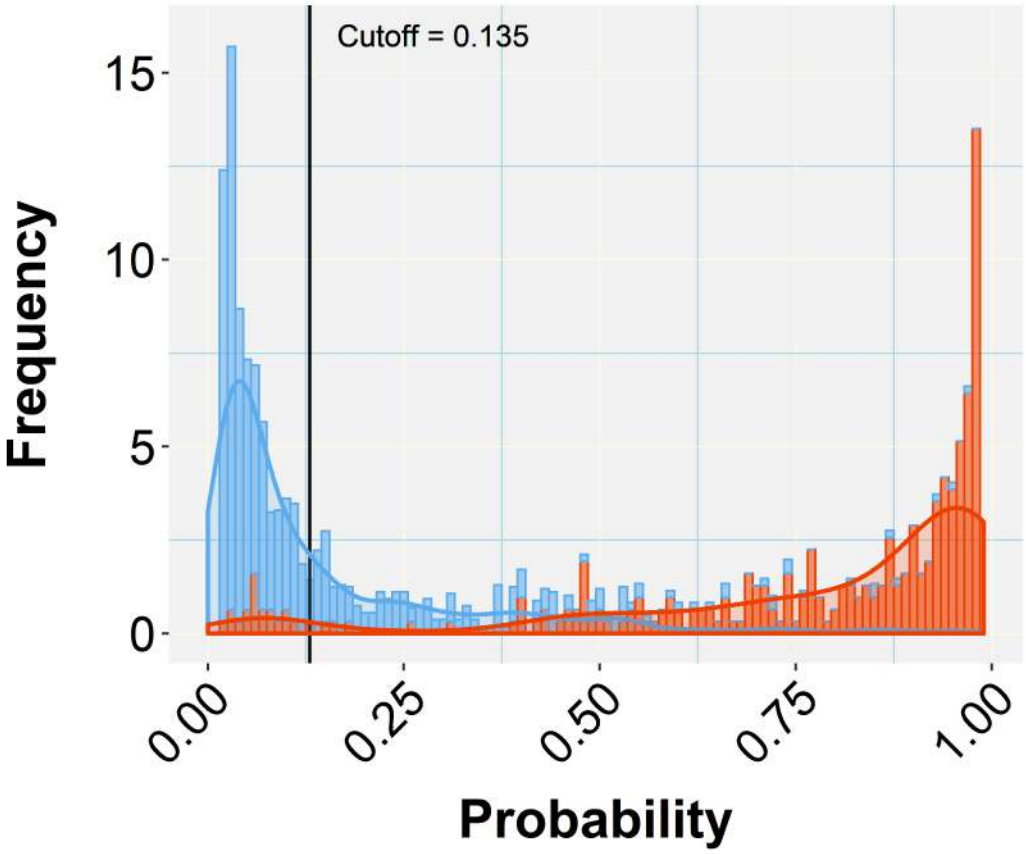
Cutoff = 0.135
Frequency
15
10
5
0
0.00
0.25
0.50
0.75
1.00
Probability

Figure 6

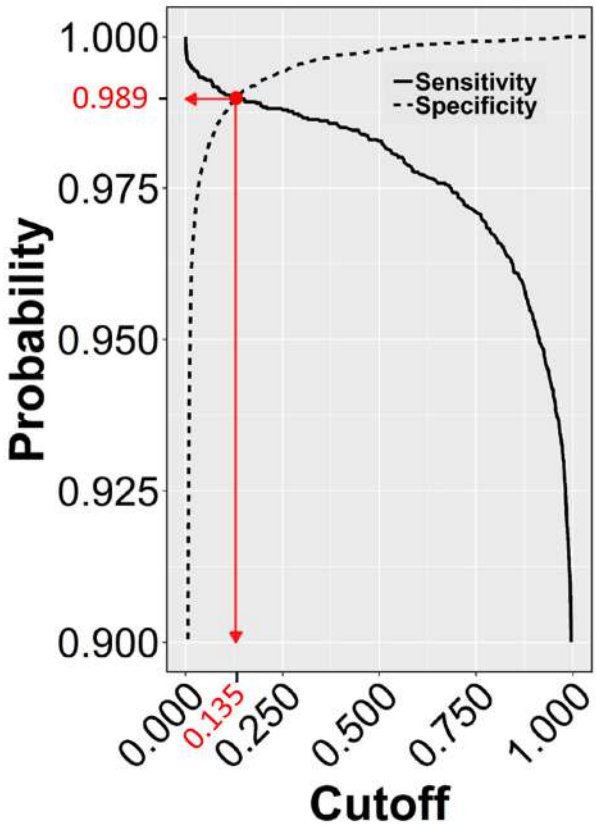
1.000
0.989
0.975
0.950
0.925
0.900
Probability
Sensitivity
Specificity
0.000
0.135
0.250
0.500
0.750
1.000
Cutoff

Figure 7

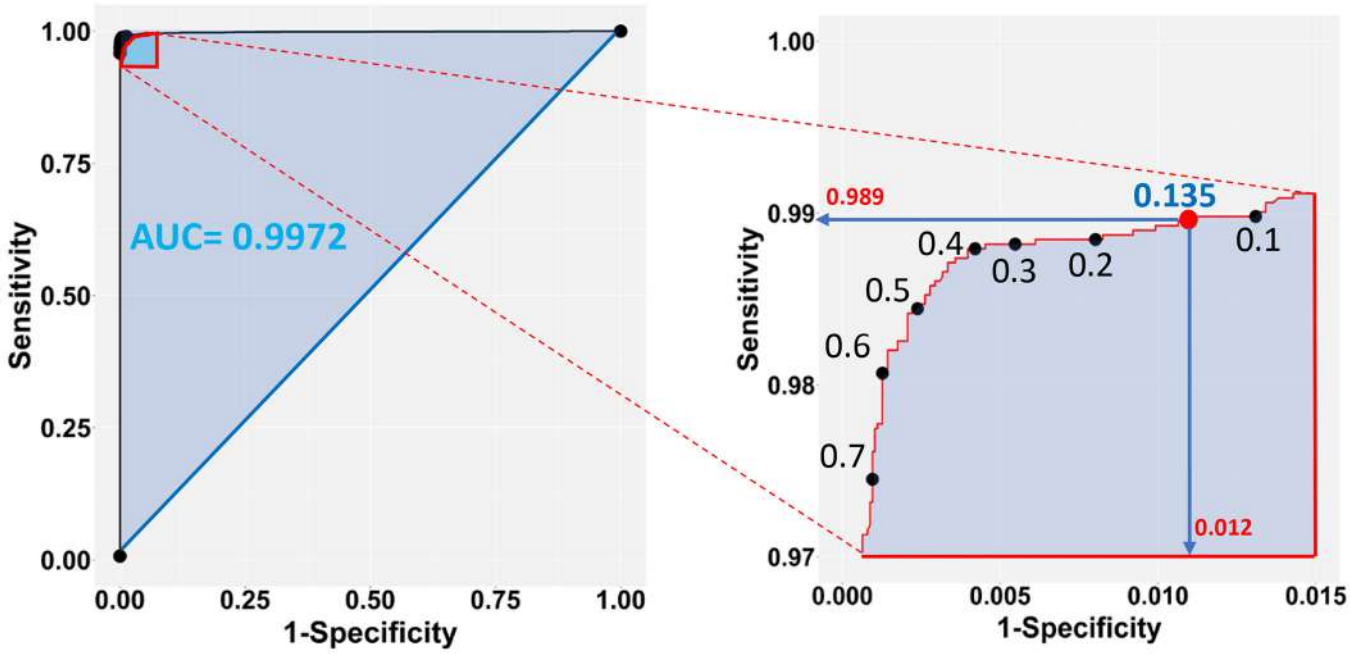
1.00
0.75
0.50
0.25
0.00
Sensitivity
AUC= 0.9972
0.00
0.25
0.50
0.75
1.00
1-Specificity
1.00
0.99
0.98
0.97
Sensitivity
0.989
0.135
0.1
0.2
0.3
0.4
0.5
0.6
0.7
0.012
0.000
0.005
0.010
0.015
1-Specificity

Figure 8

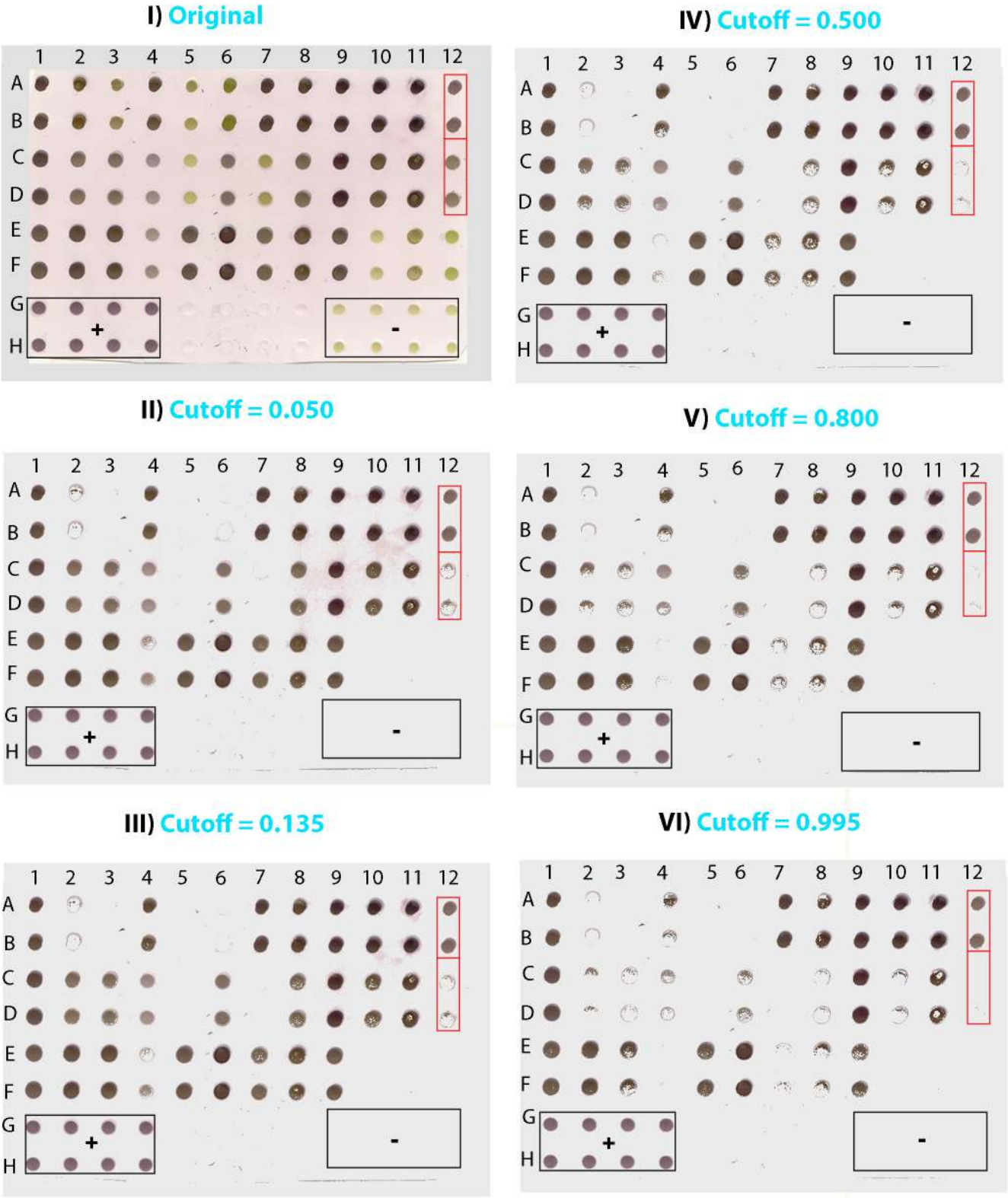
I) Original
IV) Cutoff = 0.500
II) Cutoff = 0.050
V) Cutoff = 0.800
III) Cutoff = 0.135
VI) Cutoff = 0.995
1 2 3 4 5 6 7 8 9 10 11 12
A B C D E F G H
+
-
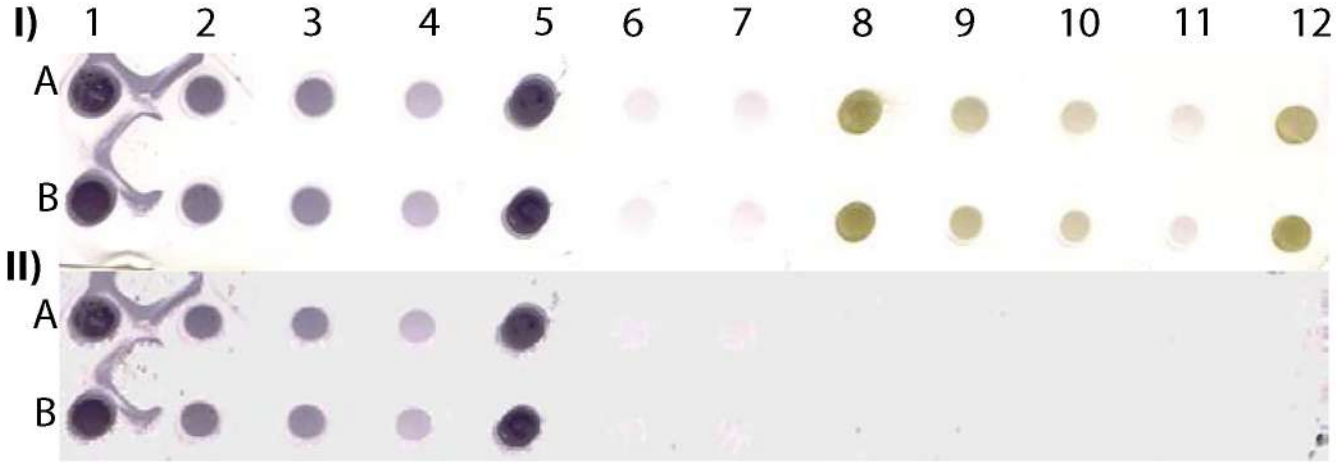
Figure 9